Environment monitoring of mining area with comprehensive mining ecological index (CMEI): a case study in Xilinhot of Inner Mongolia, China

Yuanheng Sun, Jun Li, Chengye Zhang, Feiyue Li, Wei Chen & Ying Li

Published online: 25 Apr 2023.

Submit your article to this journal

Article views: 6

View related articles

View Crossmark data

Taylor & Francis
Taylor & Francis Group

Check for updates

Environment monitoring of mining area with comprehensive mining ecological index (CMEI): a case study in Xilinhot of Inner Mongolia, China

Yuanheng Sun[a], Jun Li[b,c], Chengye Zhang[b,c], Feiyue Li[c], Wei Chen[c] and Ying Li[a]

[a]Environmental Information Institute, Navigation College, Dalian Maritime University, Dalian, China; [b]State Key Laboratory of Coal Resources and Safe Mining, China University of Mining and Technology (Beijing), Beijing, China; [c]College of Geoscience and Surveying Engineering, China University of Mining and Technology (Beijing), Beijing, China

ABSTRACT

The monitoring and evaluation of environmental and ecological status in mining area is critical for effective mineral management guidance, and remote sensing is a cost-effective solution for covering a wide spatial area with high temporal frequency. However, the diverse landscape in mining areas presents a challenge for finding a suitable monitoring method. To address this challenge, this study proposes a remote sensing-based comprehensive mining ecological index (CMEI), which integrates vegetation greenness, soil wetness, urban heat, air quality and water quality indicators obtained from Landsat images and Moderate Resolution Imaging Spectroradiometer (MODIS) products. The integration is achieved through a principal component analysis (PCA) to encapsulate various aspects of the environment in opencast mining areas. The proposed CMEI was then applied to assess the performance of an ecological restoration project carried out in the Xilinhot coalfield in Inner Mongolia, China, over the past two decades. Our findings show that the overall ecological environment in the dumping sites and backfilling sites of Xilinhot coalfield has improved from a score of 0.15 in 2005 to 0.33 in 2020, according to the CMEI. Nevertheless, our study also highlights that some newly established dumping sites require further strengthening of management and maintenance measures. The CMEI presents a novel and effective approach for monitoring and evaluating the ecological environment in mining areas, and it can potentially be applied to assess the ecological environment of opencast mining areas globally.

Introduction

Coal is a crucial natural resource and it plays the most essential role in electricity generation and industrial development in China (Yu 2017; Zhang et al. 2017; Bai et al. 2018). However, increasing opencast coal mining activities, particularly in Shanxi, Shaanxi, and Inner Mongolia, results in substantial ecological disturbances, impacting the original landform's vegetation, soil, air, and landscape (Gao et al. 2021). To mitigate the ecological consequences of mining activities, ecological restoration and management have become a crucial issue and a focus of attention for the Chinese government (Lv et al. 2019; Du et al. 2020; Wang et al. 2021). In arid and semi-arid areas with high ecological fragility where most Chinese coalfields are located, ecological restoration projects are particularly necessary.

There are two main methods for monitoring the ecological environment of mining area and evaluating the performance of ecological restoration: field survey and remote sensing observation (Hui et al. 2021; Wang et al. 2021). Field surveys have traditionally been used for monitoring and evaluating ecological environments, but they are time-consuming and labor-intensive, limiting the application of long-term and large-scale monitoring (McKenna et al. 2020). Remote sensing has led to more investigations on ecological monitoring and offers large coverage and high temporal frequency and efficiency (Li et al. 2020; Song et al. 2020), enriching and diversifying the objects, methods, and perspectives in evaluations. Thus, the use of remote sensing technology for monitoring the ecological environment and restoration performance in mining areas is highly promising (Zhang et al. 2012; Song et al. 2020; Liu et al. 2021).

The original method of ecological environment monitoring using remote sensing techniques involves various vegetation indices, with the normalized difference vegetation index (NDVI) being the most widely used one (Rouse et al. 1974). The NDVI has been utilized in many studies to monitor vegetation growth changes at different periods and to analyze the factors related to vegetation growth in mining areas (Erener 2011; Tote et al. 2014; Padmanaban et al. 2017; Yang et al. 2018). However, the NDVI gets saturated at dense vegetated condition (Sun et al. 2018, 2020) and is highly sensitive to soil background, making it unsuitable for extreme low or high vegetation coverage conditions. Other vegetation indices, such as soil-adjusted

vegetation index (SAVI) (Huete 1988), vegetation condition index (VCI) (Kogan 1995), and vegetation parameters like leaf area index (LAI) (Sun et al. 2022), have also been employed for ecological environment monitoring.

To address the limitations of vegetation indices, a more complicated remote sensing-based index that takes into consideration multiple environmental components has been proposed. For example, Xu (2013) integrates four environmental components (greenness, wetness, dryness, and heat) through principal component analysis (PCA) to generate the remote sensing-based ecological index (RSEI), which could effectively reveal regional ecological quality. The RSEI has been utilized in a variety of ecological environment monitoring applications (Xu et al. 2019; Qureshi et al. 2020; Sun et al. 2020), including in mining areas (Li et al. 2021). However, existing literatures often migrate evaluation methods from other scenes, ignoring the complex landscape features and environmental vulnerabilities in opencast mining areas (Padmanaban et al. 2017; McKenna et al. 2020; Song et al. 2020). Opencast mining areas contain multiple land cover types, making it unscientific to use the same evaluation indicators for different land cover types. Coal mining activities cause irreversible effects on the environment, such as vegetation degradation, soil quality decline, and water and air pollution (Gao et al. 2021), requiring a comprehensive consideration of various environmental components for accurate evaluation. Thus, a comprehensive remote sensing ecological environment evaluation method is crucial for opencast mining areas.

In summary, the current remote sensing monitoring methods for the ecological environment in opencast mining areas are inadequate due to their inability to accurately handle the diverse landscape there, and the development of a suitable monitoring method requires accurate land cover classification and the extraction of relevant environmental factors. To address this need, this study aims to (1) establish a preliminary standard for land cover classification in opencast mining area and (2) propose a comprehensive mining ecological index (CMEI) for the purpose of monitoring the ecological environment in mining areas. The proposed CMEI is then tested through a case study in Xilinhot, Inner Mongolia of China.

The organization of this article is outlined as follows. Section 2 describes the study area and datasets, including Landsat and MODIS products. Detailed descriptions regarding the implementation of the CMEI, including the land cover classification and indicator retrieval, are described in Section 3. The results of the ecological environment evaluation performed using the CMEI in Xilinhot are presented in Section 4. Section 5 discusses the method applicability, causes

of uncertainty, and remaining issues to be improved. This article concludes in Section 6 with a summary of the results.

Study area and materials

Study area

The study area of this research is Xilinhot, the capital of Xilin Gol League, Inner Mongolia, China. Located approximately 620 km northwest of Beijing, the city has a mid-temperate semi-arid continental climate, with an average annual temperature as 3.49°C and average annual precipitation of 278.44 mm. The majority of the rainfall occurs from June to August (Yiruhan et al. 2011). The natural vegetation in the area is mainly grassland and the terrain is hilly, with a high elevation in the south and low elevation in the north (Lyu et al. 2020), which makes Xilinhot a fragile ecosystem that is highly sensitive to climate change.

Xilinhot is abundant in mineral resources, including over 30 billion tons of proven coal reserves. Three coalfield mining sites are located within the study area, and the largest Shengli coalfield (No. 1 mining site in Figure 1), which is estimated to have 22.7 billion tons of reserves, is located approximately 10 km northwest of Xilinhot and has favorable conditions for centralized development due to its thick coal seam, shallow burial, and simple geological structure (Wu et al. 2020). In 2004, the massive mining project at Shengli coalfield was initiated and its largest-scale construction phase took place in 2006. The other two coalfield mining sites (No. 2 and No. 3 in Figure 1) share similarities with Shengli coalfield, with smaller coal reserves and limited spatial coverage. All three mining sites are opencast, which poses a direct threat to the surrounding ecological environment.

Materials

In this study, Landsat datasets, including Landsat-5 Thematic Mapper (TM), Landsat-7 Enhanced Thematic Mapper plus (ETM+), and Landsat-8 Operational Land Imager (OLI), were utilized for land cover classification and most environmental indicator retrieval. Besides, the Aqua Moderate Resolution Imaging Spectroradiometer (MODIS) daytime and nighttime land surface temperature (LST) products were also employed to calculate the day-night temperature difference of impervious surfaces.

Landsat data

High standard atmospherically corrected surface reflectance (SR) datasets acquired from Landsat-5, Landsat-7, and Landsat-8 during the summer of 2005, 2010, 2015, and 2020 were employed in this study. The spatial resolution of the Landsat images is 30 m, and
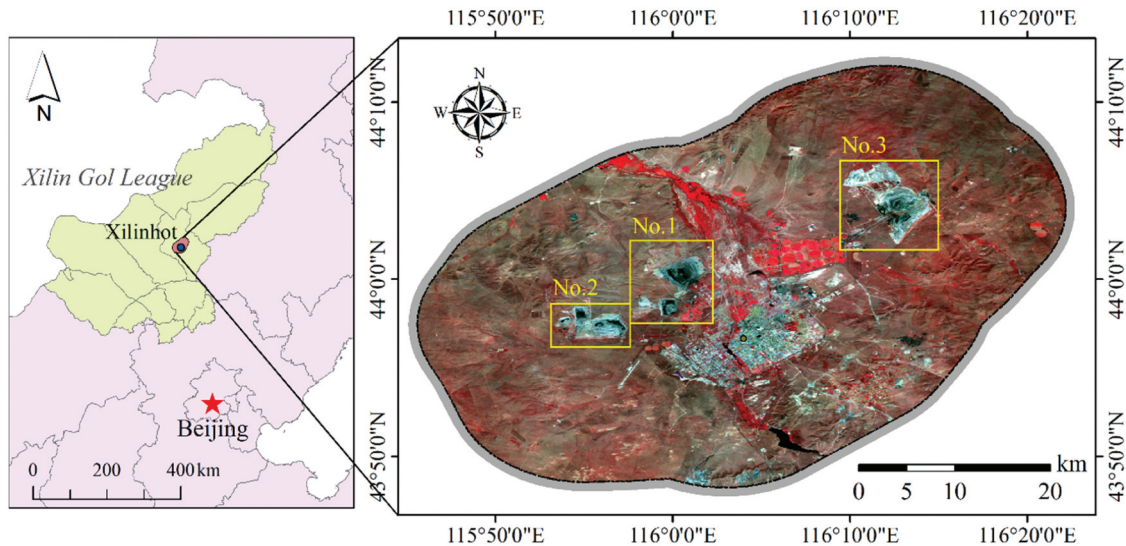
Figure 1. Location of the study area – Xilinhot, in a map of northern China. The background imagery on the right-hand side enlarged map is from false-color composite Sentinel-2 multispectral images in the summer of 2021. Three coalfield mining sites within the study area are marked with yellow squares.

the temporal resolution is 16 days. The datasets have been atmospherically corrected using either the LaSRC (for Landsat-8) or LEDAPS (for Landsat-5 and 7) algorithms, and they include a cloud, shadow, water, and snow mask generated using CFMASK, as well as a per-pixel saturation mask (Zhu et al. 2015). The Landsat-8 OLI has five visible and near-infrared (VNIR) and two short-wave infrared (SWIR) bands, while Landsat-5 TM and Landsat-7 ETM+ contain four VNIR and two SWIR bands, which are all processed to orthorectified SR. Only the VNIR bands were utilized for environmental indicator retrieval. The detailed spectral range of each band for each sensor is listed in Table 1. The spectral ranges of the blue, green, and red bands of the TM/ ETM+ and OLI are similar; however, difference appears in the NIR band. The narrower width of the OLI NIR band reduces the impact of aerosol contamination, leading to a more stable NIR signal from the land surface.

The pre-processing of the Landsat datasets involved two steps. First, pixels contaminated by clouds and cloud shadows were removed by consulting the Landsat quality control band. Second, monthly composite surface reflectance for the years 2005, 2010, 2015, and 2020 was generated using the mean composite algorithm, which was calculated as the average of all available Landsat observations for each band in a specific month of each year. The time-series Landsat images for all 12 months of the year were used for land cover classification, and monthly composite surface reflectance of August was used for most environmental indicators' retrieval. Due to a large portion of the study area had invalid values in August 2005, Landsat observations from the last half of July and the first half of September were also included in the summer surface reflectance composite for 2005.

MODIS product

Daytime and nighttime land surface temperature (LST) data from C6 (collection 6) Aqua MODIS LST and emissivity product (MYD11A2) was utilized in this study to quantify the day and night temperature difference for impervious surfaces. The data covers the summer months of 2005, 2010, 2015, and 2020. The MYD11A2 measures the temperature of Earth's surface thermal emission at local times of approximately 13:30 and 01:30, which are believed to provide the highest and lowest LST during a day compared to other MODIS LST measurements. Eight-day composite LST values were derived from the MYD11A2 product by averaging the values from the corresponding daily files and were projected onto a 1-km sinusoidal grid (Wan 2014).

The monthly composite LST of the relevant year in August was obtained by taking the maximum value composite of the 8-day MYD11A2 LST product. The LST dataset was in a 1-km sinusoidal grid format, which was then transformed into a WGS-1984 UTM coordinate system. The spatial resolution of the data was resampled to 30 m to match the Landsat images.

Table 1. Bands setting in VNIR for TM, ETM+, and OLI sensors.

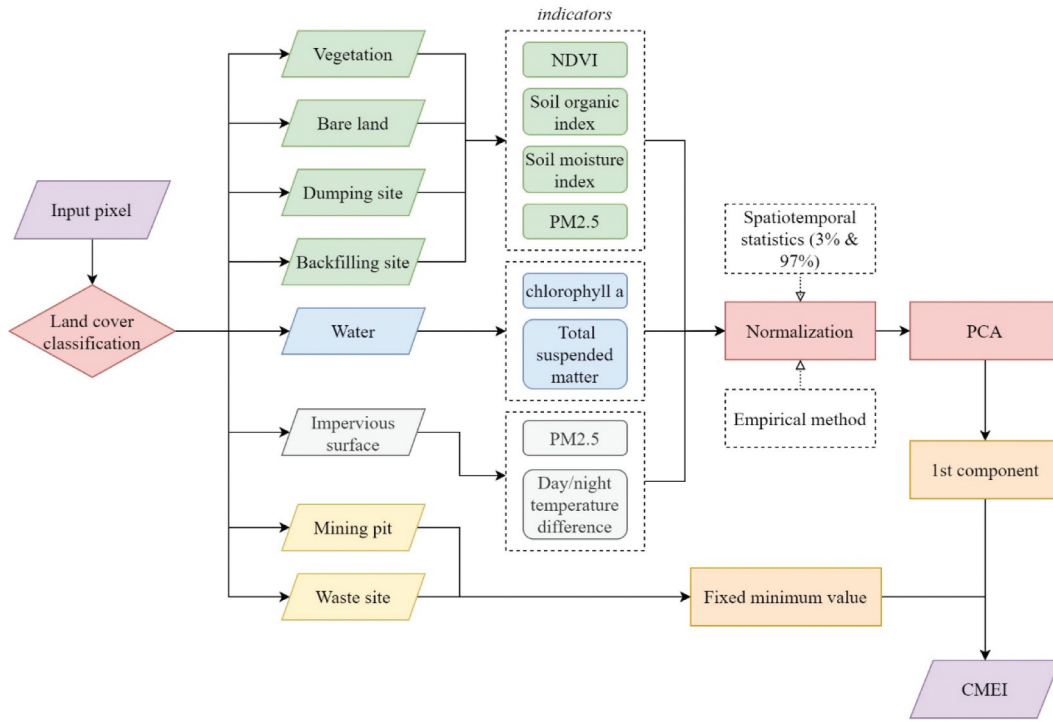| Band name	Landsat-5 TM & Landsat-7 ETM+	Landsat-8 OLI
Blue	0.45–0.52 μm (B1)	0.45–0.51 μm (B2)
Green	0.52–0.60 μm (B2)	0.53–0.59 μm (B3)
Red	0.63–0.69 μm (B3)	0.64–0.67 μm (B4)
NIR	0.77–0.90 μm (B4)	0.85–0.88 μm (B8)

Figure 2. Workflow of comprehensive mining ecological index (CMEI) calculation.

Methods

The procedures for calculating the comprehensive mining ecological index (CMEI) in mining areas consist of the following steps: (1) land cover classification, (2) retrieval of environmental indicators, (3) normalization of indicators, and (4) principal component analysis. The entire workflow is illustrated in Figure 2.

Land cover classification

In this study, a preliminary land cover classification scheme was proposed for the semi-arid regions where opencast mines are prevalent, as existing land cover and land use products and technical standards have not taken into account the unique land cover types found in mining areas, such as dumping sites. The scheme includes the basic land cover types of vegetation, water, impervious surface, and mine. The vegetation land cover type was further divided into forest, grassland, farmland, bare land, mine dumping site, and backfilling site. Bare land is defined as an area where the duration of no vegetation growth exceeds a threshold in a given year, and it may have a short period of vegetation growth in the growing season. The mine type was sub-divided into mining pit and waste site.

Land cover in the study area for the years 2005, 2010, 2015, and 2020 was generated using time-series Landsat images and the maximum likelihood classification algorithm. The training samples were stratified using *in-situ* investigation and interpretation of multi-temporal, high-spatial resolution Google Earth

images, with approximately 600 samples collected for each year. The inputs for the classification model were time-series multispectral Landsat surface reflectance over an entire year with a temporal interval of half a month. The output was the land cover type, with 70% of the samples used for training and 30% for validation. Finally, some misclassified pixels located in land cover transition zones were manually modified to improve overall accuracy.

Retrieval of environmental indicators

Vegetation and bare land
Various remotely sensed indicators were utilized to assess the ecological environment from the perspective of vegetation growth, soil moisture, and soil organic status for vegetation and bare land. The specific indices employed for this purpose will be described later. Additionally, an air quality indicator is also considered, and its retrieval method will be outlined in section 3.2.3.

The NDVI was utilized as an indicator of vegetation growth status. It is a commonly used vegetation index for vegetation dynamic monitoring and is calculated as the difference between reflectance in NIR and red spectral bands, normalized by their sum. The NDVI equation is defined as follows (Rouse et al. 1974):

$$NDVI = \frac{\rho_{NIR} - \rho_{Red}}{\rho_{NIR} + \rho_{Red}} \# \tag{1}$$

where ρ_{NIR} is the surface reflectance of the NIR band and ρ_{Red} is the surface reflectance of the red band. The red and NIR bands correspond to band 3 and band 4

for Landsat-5 TM and Landsat-7 ETM+, respectively, and in Landsat-8 OLI they correspond to band 4 and band 5. Despite the observed discrepancy in NDVI values derived from different Landsat sensors, the magnitude of this difference is minimal and falls within an acceptable range for our specific application (Vogelmann et al. 2001; Roy et al. 2016; Huang et al. 2021).

The modified perpendicular drought index (MPDI) was utilized to assess soil moisture conditions (Ghulam et al. 2007). This index takes into account the fractional vegetation coverage (FVC) and minimizes the influence of vegetation to a certain extent. It measures the distance between a pixel and the soil line in the red-NIR reflectance feature space. The equation for MPDI is as follows:

$$MPDI = \frac{\rho_{Red} + M \cdot \rho_{NIR} - f_v \left(\rho_{Red,v} + M \cdot \rho_{NIR,v} \right)}{(1 - f_v)\sqrt{M^2 + 1}} \# \tag{2}$$

where ρ_{NIR} and ρ_{Red} are the surface reflectance of the NIR and red bands, respectively. M represents the slope of the soil line in the red-NIR spectral space, and f_v is the FVC of the specific pixel. The values of $\rho_{Red,v}$ and $\rho_{NIR,v}$, which represent the red and NIR surface reflectances of pure vegetation pixel, were set as 0.05 and 0.50, respectively, as recommended by the index proposer for quick application with acceptable accuracy (Ghulam et al. 2007). The slope of the soil line, M, was automatically calculated as per reference (Qin et al. 2012), and the FVC was estimated using a dimidiate pixel model with NDVI as follows:

$$f_v = \left(\frac{NDVI - NDVI_{min}}{NDVI_{max} - NDVI_{min}} \right)^2 \# \tag{3}$$

where $NDVI_{min}$ and $NDVI_{max}$ represent the NDVI values of completely bare land pixel and fully covered vegetated pixels in the study area. In this study, we used the 3% and 97% values of the NDVI statistical histogram over the study area to represent $NDVI_{min}$ and $NDVI_{max}$, with values of 0.25 and 0.84, respectively.

The normalized difference soil index (NDSI) was used as the indicator of soil organic matter (Deng et al. 2015). It was calculated as the difference between the reflectances at NIR and blue spectral bands normalized by their sum:

$$NDSI = \frac{\rho_{NIR} - \rho_{Blue}}{\rho_{NIR} + \rho_{Blue}} \# \tag{4}$$

where ρ_{NIR} and ρ_{Blue} represent the surface reflectance of NIR and blue bands.

Water

The chlorophyll-a concentration and total suspended matter (TSM) concentration, which are widely used in studies of water quality assessment (Bilotta et al. 2012; Ansper and Alikas 2019), were adopted as indicators of inland water quality. The retrieval algorithm employed was multi-layer back-propagation (BP) neural

networks, with in-situ measurements of chlorophyll-a and TSM concentrations serving as the training dataset. The inputs of the model were the blue, green, red, and NIR band surface reflectance values of Landsat imagery, while chlorophyll-a and TSM concentrations were treated as outputs. The S-curve hyperbolic tangent function was used as the transfer function in the hidden layer of the BP neural networks, while a linear function was utilized in the output layer. The maximum number of training epoch was set to 1000, with a learning rate of 0.001. To expedite convergence of the model and improve its generalization, the inputs and outputs were standardized to the range of −1 to 1 using a maximum-minimum normalization method.

Air quality

The concentrations of PM2.5 and PM10 were selected to represent air quality and employed as environmental indicators for vegetation, bare land, and impervious surface land cover types. They were estimated using a combination of Landsat remotely sensed imagery, meteorological data, and ground-based synchronized PM2.5 and PM10 observations, with a geographically weighted regression model. The aerosol optical depth (AOD) was first retrieved from Landsat data using a combination of dark object and deep blue algorithms, which effectively improved the accuracy and spatial coverage of the AOD (Sorek-Hamer et al. 2015). The geographically weighted regression model not only showed the global variations in spatial characteristic of PM2.5 and PM10 but also took local diversity into account, resulting in better performance compared to a traditional multi-linear regression model.

Impervious surface

The concentration of PM2.5, PM10, and day/night temperature difference were chosen as the environmental indicators for impervious surfaces. The day/night temperature difference was calculated as the difference between daytime and nighttime land surface temperature (LST) derived from the MODIS LST product as equation (5):

$$\Delta T = LST_{day} - LST_{night} \# \tag{5}$$

where LST_{day} represents daytime LST and LST_{night} represents nighttime LST.

Normalization of indicators

The normalization of environmental indicators was performed to standardize the values of each parameter between 0 and 1, enabling comparative analysis between indicators. The higher the normalized value of the indicator, the better the ecological quality it represents. Conversely, a lower value indicates lower ecological quality.

For parameters positively correlated with ecological quality, such as NDVI and NDSI, the normalization equation is given as follows:

$$X_{nor} = \begin{cases} 0 & X \leq X_{min} \\ \frac{X - X_{min}}{X_{max} - X_{min}} & X_{min} < X < X_{max} \\ 1 & X \geq X_{max} \end{cases} \#$$ (6)

where X represents the original value of the parameter prior to normalization, X_{nor} is the normalized value, which falls within the range of 0 to 1. X_{min} represents the minimum threshold value of the parameter during normalization (below which the ecological quality is the worst), and X_{max} represents the maximum threshold value of the parameter.

For parameters negatively correlated with ecological quality, such as MPDI, water chlorophyll-a concentration, water TSM concentration, PM2.5 and PM10 concentration, and day/night temperature difference, the normalization equation is as follows:

$$X_{nor} = \begin{cases} 1 & X \leq X_{min} \\ \frac{X_{max} - X}{X_{max} - X_{min}} & X_{min} < X < X_{max} \\ 0 & X \geq X_{max} \end{cases} \#$$ (7)

where X represents the original value of the parameter, X_{nor} represents the normalized value within the range of 0 to 1. X_{min} represents the minimum threshold value of the parameter (below which the ecological quality is the best), and X_{max} represents the maximum threshold value of the parameter (above which the ecological quality is the worst).

The minimum and maximum thresholds for NDVI and NDSI were derived from the multi-year statistics of the spatial and temporal distributions of these parameters in the study area. The minimum threshold for NDVI was set as 0.15 and the maximum as 0.84, while for NDSI, the minimum was set as 0.1 and the maximum as 0.65. The minimum and maximum thresholds for MPDI were established based on the multi-year spatiotemporal statistics of the study area and typical MPDI values in literature (Zhang et al. 2015), with a minimum of 0.05 and a maximum of 0.77. The thresholds for PM2.5 and PM10 were set according to the Ambient Air Quality Standards of China (GB3095–2012), with a minimum of 5 $\mu g/m^3$ and maximum of 75 $\mu g/m^3$ for PM2.5 and a minimum of 10 $\mu g/m^3$ and a maximum of 150 $\mu g/m^3$ for PM10. Despite the temperature difference derived from MODIS LST differed from that of air temperature, its relative value was still meaningful, and its thresholds were determined based on multi-year spatial and temporal distributions of this parameter in the study area, with a minimum of 25°C and a maximum of 40°C. The minimum and maximum thresholds for water chlorophyll-a concentration were determined based on typical values in literature, with a minimum of 5$\mu g/L$ and a maximum of 80$\mu g/L$, while the minimum and maximum thresholds for water TSM concentration were set as 10mg/L and 120mg/L,

respectively, based on related references (Bilotta et al. 2012; Ansper and Alikas 2019).

CMEI calculation

Principal component analysis (PCA) was further employed to generate the comprehensive mining ecological index (CMEI) by normalizing environmental indicators for each land cover type. For mine land cover type, which includes mining pit and wasted site, a CMEI of 0 was assigned directly. The first component of PCA result was considered as the CMEI, and it was calculated as follows:

$$Y = \sum_{i=1}^{n} k_i \times X_i \#$$ (8)

Here, X_i represents the ith normalized indicator of a specific land cover type, and k_i represents the weight of indicator i of the first component after the PCA process. For vegetation, bare land, mine dumping sites and backfilling site, $n = 5$ and the input indicators are normalized NDVI, MPDI, NDSI, PM2.5, and PM10. For impervious surface, $n = 3$ and the input indicators are normalized day/night temperature difference, PM2.5, and PM10. For water body, $n = 2$ and the input indicators are normalized chlorophyll-a concentration and TSM concentration.

The resulting CMEI values of different land cover types were ultimately spatially combined to generate a comprehensive CMEI map of the entire study area.

Results

Land cover changes over the study area

Figure 3 displays the land cover changes in the study area from 2005 to 2020. The Shengli coalfield was the only operating mining site in 2005, while two additional mining sites emerged by 2010. The mining and bare land in the eastern part of the study area have shown an expansion trend with the direction of expansion changing from east and north between 2005 and 2010 to west between 2010 and 2015. Vegetation restoration occurred at the same time with the expansion of mining land and bare land, leading to the formation of dumping sites (yellow color in Figure 3) in the area. The dumping site is an ecologically fragile area where ecological restoration projects have been mainly carried out. The grassland has decreased due to the expansion of mining and impervious surface, while the spatial distribution of other land cover types such as forest, cropland, and inland water has remained stable.

To quantify land cover changes of Xilinhot from 2005 to 2020, we calculated the percentage of each land cover type over the study area for the 4 years and presented the results in Table 2. Grassland covered the majority of the area and it decreased from 90.18% in
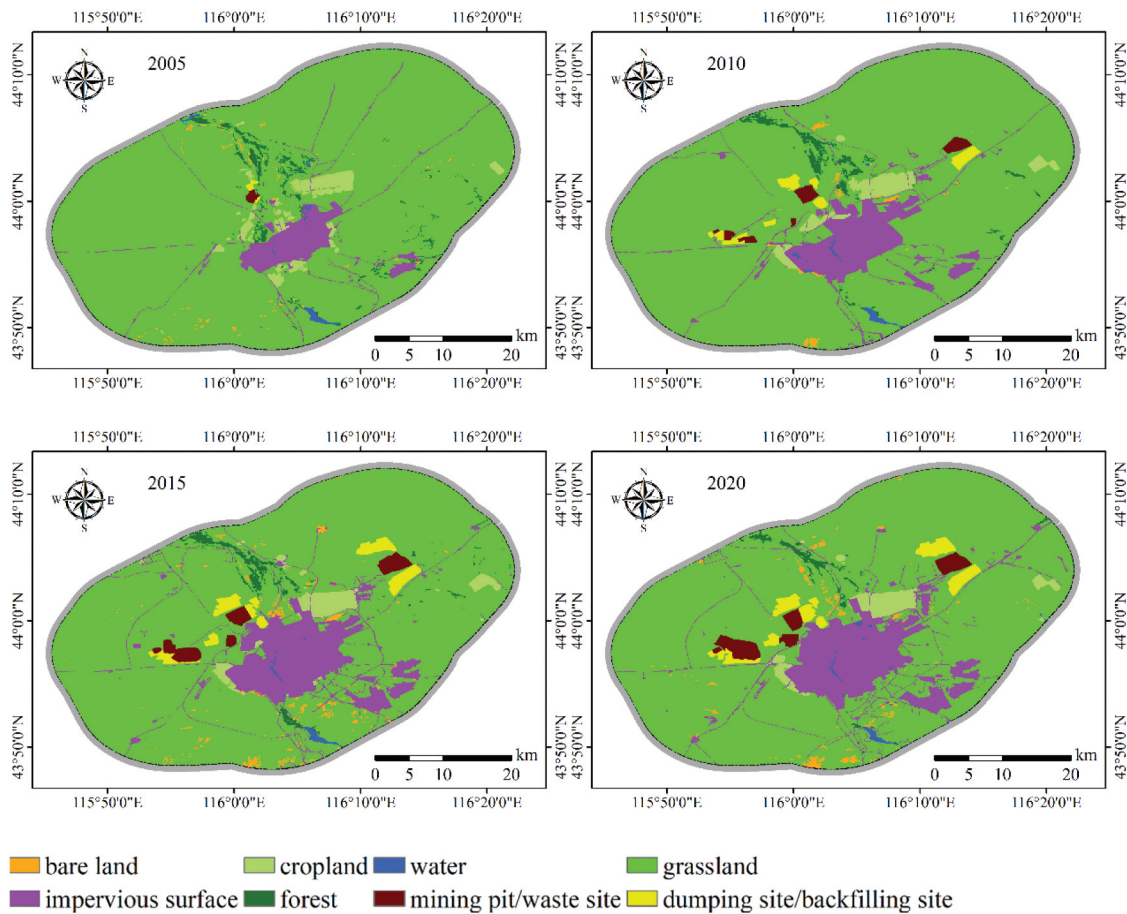
legend:
- bare land
- cropland
- water
- grassland
- impervious surface
- forest
- mining pit/waste site
- dumping site/backfilling site

Figure 3. Spatial distribution of land cover types across the study area according to the proposed mining area land cover classification scheme for 2005, 2010, 2015 and 2020.

Table 2. Percentage of each land cover type over the study area for 4 years.

	2005	2010	2015	2020
bare land	0.38	0.40	1.13	0.91
impervious surface	4.81	8.11	11.25	12.01
cropland	2.48	2.24	2.18	2.07
forest	1.63	1.41	1.38	1.33
water	0.31	0.28	0.25	0.28
grassland	90.18	85.60	80.35	79.35
dumping site/backfilling site	0.09	1.11	1.95	2.26
mining pit/waste site	0.12	0.85	1.51	1.79

2005 to 79.35% in 2020. Impervious surfaces significantly increased from 4.81% in 2005 to 12.01% in 2020, resulting in the decline of grassland. Urbanization was the main driving force for the increase in impervious surface area. Mining-related land cover changes, including the expansion of mining sites, dumping sites, and backfilling sites, also showed an overall upward trend, increasing from 0.21% in 2005 to 4.05% in 2020 (Table 2). Cropland and inland water remained relatively constant due to strict protection policies in China for farmland and the high value of water resources in the semi-arid region.

Spatial and temporal variations of CMEI

The CMEI proposed by this work was utilized to quantitatively evaluate the ecological environment quality of the study area. Figure 4 displays the spatial and temporal distribution of CMEI in Xilinhot, revealing that forest and cropland exhibit the highest ecological quality with CMEI. This is due to the dominant weight assigned to vegetation greenness in CMEI calculation for these basic land cover types, which is notably greater than other land cover types. The urban area of impervious surface ranked the second highest with a suitable temperature difference and air quality for human settlements. The CMEI value of grassland and mine dumping and backfilling sites varied spatially and temporally, because they were largely dependent on vegetation and soil status.

The CMEI value of bare land remained relatively constant over the 4-year period with a range of 0.33 to 0.39. The stable performance of CMEI over the years indicates the reliability of the CMEI as there was no systematic management for bare land, such as soil
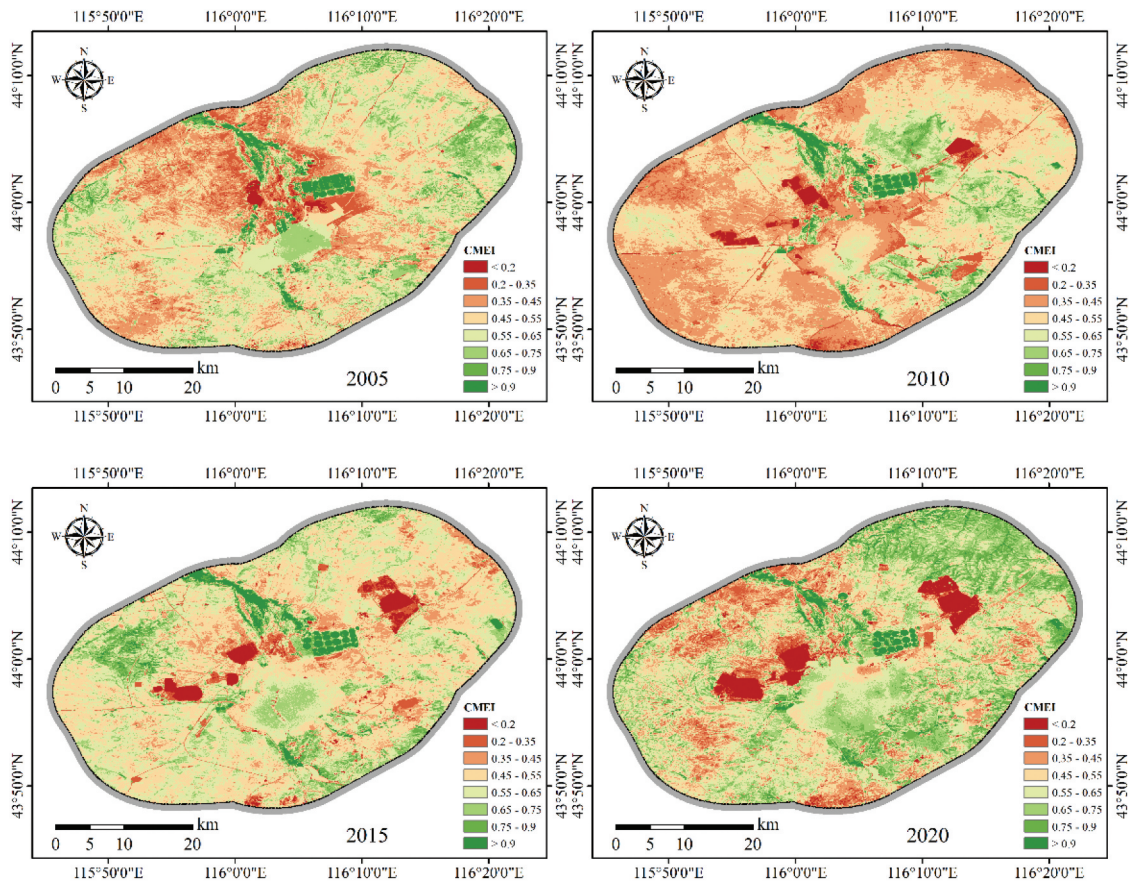
Figure 4. Spatial distribution of CMEI across the study area for 2005, 2010, 2015 and 2020.

fertilization, in the study area during the past two decades. Forest and cropland exhibited the highest CMEI with a mean value of 0.84 to 0.96, with little variation except for an abnormal low value of the forest in 2005, which might have been caused by the relatively low quality of Landsat data during that period.

The ecological environment quality of grassland gradually increased from 0.53 to 0.59 over the years, even though its area has been shrinking continuously. The most significant increment of CMEI occurred in mining dumping and backfilling sites, from 0.15 in 2005 to 0.33 in 2020. Ecological restoration projects have been implemented in these sites, promoting the ecological quality from a very low level to a level as that of bare land. Regarding the effect of ecological restoration, the closer it is to the mining pit, the worse the effect will be, mainly because the vegetation restoration work started from the furthest distance and moves progressively towards the pit. Therefore, the earlier the vegetation restoration work began, the more time the vegetation had to grow and develop, resulting in better vegetation quality. After the vegetation restoration work is completed, the area closer to the mine is more likely to be affected by human activities, increasing the probability of degradation.

In the next section, a specific coalfield mining site, Shengli coalfield (No. 1 mining site in Figure 1), will be

analyzed as an example to investigate how ecological quality changes in dumping and backfilling sites with the ecological restoration projects implemented, using CMEI as the indicator.

CMEI dynamics on mine dumping site with ecological restoration

The Shengli coalfield, the largest one in the study area, was selected as an example to investigate the dynamics of the CMEI during the ecological restoration process of mine-dumping sites. Mining operations began in 2004, and by 2005, two small dumping sites (B1 and B2 in Figure 5) had appeared in the north and southeast of the mining pit. The CMEI value of these dumping sites was very low, indicating poor ecological quality at that time. Five years later in 2010, the area of mining pit and dumping sites had greatly expanded, and a new dumping site (B3 in Figure 5) emerged in the northwest of the pit. At the same time, a new mining pit (A2 in Figure 5) and dumping site (B4 in Figure 5) were under construction in the southwest of the mining area. During this period, ecological restoration on dumping sites began with the planting of tree and grass to reduce soil exposure. The CMEI value of dumping site B1 dramatically increased to 0.55 by 2010 compared with 2005, and that of dumping site B2 slightly increased to about 0.21 (Figure 6).
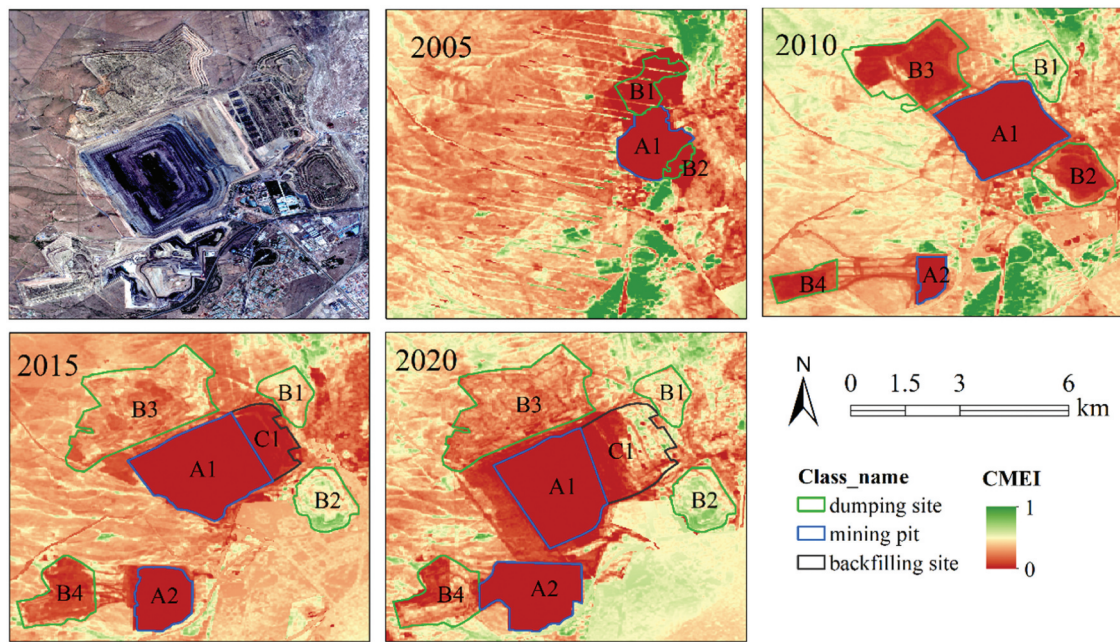
Figure 5. Specific land cover transformations and CMEI dynamics of No.1 mining site for 2005, 2010, 2015 and 2020. The mining pits and dumping sites have been expanding for the past 20 years due to the mining activities. with the implementation of ecological restoration policy, the ecological condition of dumping sites and backfilling site was getting better revealed by multi-year CMEI. The upper-left high-resolution image of No. 1 mining site captured in the spring of 2021 is from Google Earth.

In 2015, the most significant CMEI increment occurred in mine dumping site B2, which may have been the focus of the ecological restoration project, with its CMEI value increasing from 0.21 in 2010 to 0.66 in 2015 (Figure 6). Dumping site B1 maintained a high level of ecological quality, with a constant CMEI value of 0.55. The CMEI value of dumping site B3 and B4 also increased as their areas expanded. With the massive exploitation of the mining pit A1, the early-stage exploitation area began to backfill with soil and stone, forming the backfilling site, another important target of ecological restoration. In 2020, the area of backfilling site C1 expanded significantly, and its CMEI value increased from 0.17 to 0.27 due to ecological restoration (Figure 6). The CMEI value of the mine dumping sites remained stable or slightly decreased
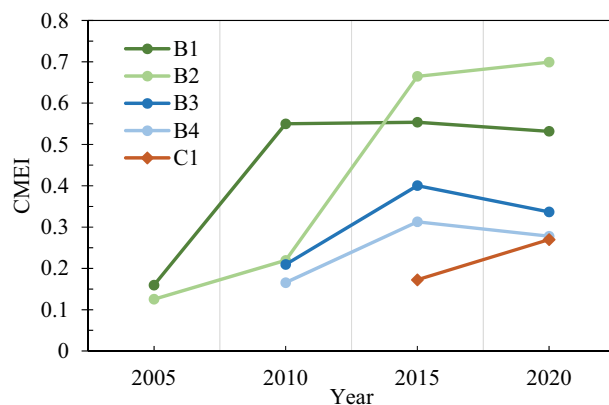
in 2020. Some of these sites (B1 and B2) were already in a mature restored status, with relatively high CMEI values and ecological quality, while others (B3 and B4) were still in the process of restoration.

Discussion

Effective monitoring and assessment of ecological restoration performance in mining areas is essential for mining management (Du et al. 2020), and remote sensing offers a promising solution to this problem as it is convenient and cost-effective (Padmanaban et al. 2017; Li et al. 2020). Remote sensing monitoring has advantages such as regularity, easy access, and providing rich information. In contrast, records of land reclamation work by enterprises are often unreliable, making remote sensing monitoring more objective and reliable (Hui et al. 2021). However, the use of remote sensing for ecological restoration monitoring is still challenging due to issues related to remotely sensed data acquisition, indicator selection, and interpretation.

This article proposes a comprehensive mining ecological index (CMEI) based on remote sensing data for ecological environment monitoring in mining areas and applied it to the ecological restoration project assessment of mining areas in Xilinhot, Inner Mongolia of China. The CMEI proposed in this paper not only considers the vegetation and soil indicators commonly used in previous studies (Padmanaban et al. 2017; Song et al. 2020) but also incorporates indicators reflecting water and air

Figure 6. CMEI dynamics of each dumping site or backing filling site across Shengli coalfield (No. 1 mining site).

pollution through a principal component analysis method, thus reflecting the overall ecological environment status and changes over time. Another vital feature of the CMEI is that it takes into account the diversity of landscape features in opencast mining areas, and the relevant environmental indicators are chosen for different land cover types, which improves the accuracy of ecological assessment.

Despite the promising performance of CMEI, there are still rooms for improvement. The accuracy and effectiveness of CMEI depend on accurate land cover classification. A maximum likelihood algorithm was used in this study, but the classification accuracy is limited, especially in boundary regions with land cover-type transitions. More advanced machine learning methods, such as deep learning algorithms, could be used to improve classification accuracy automatically (Hong et al. 2021). The retrieval accuracy of each indicator also significantly affects the performance of CMEI. Therefore, it is crucial to select appropriate indicators for each land cover type to reduce the error propagation as much as possible. Furthermore, the discrepancy in the spatial resolution of Landsat derived indicators (e.g. NDVI) and MODIS derived indicators (e.g. day/night temperature difference) may jeopardize the spatial continuity and accuracy of the result, necessitating the use of high spatial resolution temperature or temperature indicators. Additionally, the thresholds used in indicator normalization are still empirical and require further testing for their applicability in other areas.

The multi-year evaluation of the Xilinhot mining area revealed an overall improvement in the ecological environment, consistent with previous research findings (Fu et al. 2017; Li et al. 2023). The mine pits experienced the fastest degradation rate, which was attributable to the massive mining activities. Moreover, other artificial factors such as grazing and ecological restoration may also have impacts on the change in the CMEI, but they were difficult to quantify. For specific mine dumping site where ecological restoration project carried out, the improvement was significant. The ecological restoration project carried out in a specific mine dumping site led to remarkable improvements. The Shengli coalfield initiated the ecological restoration project in 2006 and completed its first round by 2013. A new round of ecological restoration began in 2016, consistent with the changes in the CMEI of the dumping and backfilling sites (B1 and C1 in Figure 6). Some dumping sites (B1 and B2 in Figure 5) in the Shengli coalfield have attained a stable high ecological level, indicating the success of the restoration project. However, other methods (B3 and B4 in Figure 5) have not reached the ultimate stage, requiring more attention during the subsequent restoration project. While the ecological restoration may have mitigated the negative impact of mining on vegetation, the results confirm its effectiveness.

The construction and operation of the CMEI align with the goals of regional sustainable development (SDGs) of the United Nations (UN) (Moomen et al. 2019). Since CMEI only needs to be calculated through satellite images, it has the potential to realize the evaluation of the ecological environment of various opencast mining areas at a large scale and to reveal the current status of the ecological environment in opencast mining areas. In this sense, the ecological environment status of global opencast mining areas would be clarified and can be updated year-by-year, which is of great significance for global sustainable development.

Conclusion

This study proposes a comprehensive mining ecological index (CMEI) for ecological environment monitoring in opencast mining areas using remote-sensing data. The CMEI takes into account various environmental indicators, such as greenness, wetness, heat, air quality, and water quality, which are normalized and processed through PCA to extract the first component as CMEI. Compared with existing remote sensing-based indices for the ecological environment monitoring, the proposed CMEI incorporates indicators reflecting water and air pollution, considers the characteristics of different land cover types and can be calculated through satellite images, enabling large-scale and comprehensive evaluation of the ecological environment. The evaluation of the Xilinhot mining areas using CMEI reveals that the ecological environment of coalfield dumping sites and backfilling sites has improved over the past 15 years, while the ecological environment of other land types has remained stable. The dumping site and backfilling site of Shengli coalfield were specifically assessed, and the CMEI showed a stepwise increment over time. The CMEI has the potential to evaluate global opencast mining areas quickly and efficiently, clarifying their ecological environment status and contributing to global sustainable development, and accurate land cover classification and suitable choice of environmental indicators for different land cover types still require further exploration to improve the performance of CMEI.

References

Ansper A, Alikas K. 2019. Retrieval of chlorophyll a from sentinel-2 MSI data for the European Union water framework directive reporting purposes. Remote Sensing. 11 (1):64. doi:10.3390/rs11010064.

Bai XF, Ding H, Lian JJ, Ma D, Yang XY, Sun NX, Xue WL, Chang YJ. 2018. Coal production in China: past, present, and future projections. Int Geol Rev. 60(5–6):535–547. doi:10.1080/00206814.2017.1301226.

Bilotta GS, Burnside NG, Cheek L, Dunbar MJ, Grove MK, Harrison C, Joyce C, Peacock C, Davy-Bowker J. 2012. Developing environment-specific water quality guidelines for suspended particulate matter. Water Res. 46 (7):2324–2332. doi:10.1016/j.watres.2012.01.055.

Deng YB, Wu CS, Li M, Chen RR. 2015. RNDSI: a ratio normalized difference soil index for remote sensing of urban/suburban environments. Int J Appl Earth Obs. 39:40–48. doi:10.1016/j.jag.2015.02.010.

Du T, Wang DM, Bai YJ, Zhang ZZ. 2020. Optimizing the formulation of coal gangue planting substrate using wastes: the sustainability of coal mine ecological restoration. Ecol Eng. 143:105669. doi:10.1016/j.ecoleng.2019.105669.

Erener A. 2011. Remote sensing of vegetation health for reclaimed areas of Seyitömer open cast coal mine. Int J Coal Geol. 86(1):20–26. doi:10.1016/j.coal.2010.12.009.

Fu X, Ma MF, Jiang P, Quan Y. 2017. Spatiotemporal vegetation dynamics and their influence factors at a large coal-fired power plant in Xilinhot, Inner Mongolia. Int J Sust Dev World. 24(5):433–438. doi:10.1080/13504509.2016.1273265.

Gao Y, Wang JM, Zhang M, Li SJ. 2021. Measurement and prediction of land use conflict in an opencast mining area. Resour Policy. 71:101999. doi:10.1016/j.resourpol.2021.101999.

Ghulam A, Qin QM, Teyip T, Li ZL. 2007. Modified perpendicular drought index (MPDI): a real-time drought monitoring method. ISPRS J Photogramm. 62(2):150–164. doi:10.1016/j.isprsjprs.2007.03.002.

Hong DF, Gao LR, Yokoya N, Yao J, Chanussot J, Du Q, Zhang B. 2021. More diverse means better: multimodal deep learning meets remote-sensing imagery classification. IEEE T Geosci Remote. 59(5):4340–4354. doi:10.1109/TGRS.2020.3016820.

Huang S, Tang LN, Hupy JP, Wang Y, Shao GF. 2021. A commentary review on the use of normalized difference vegetation index (NDVI) in the era of popular remote sensing. J Forestry Res. 32(1):1–6. doi:10.1007/s11676-020-01155-1.

Huete AR. 1988. A soil-adjusted vegetation index (SAVI). Remote Sens Environ. 25(3):295–309. doi:10.1016/0034-4257(88)90106-x.

Hui JW, Bai ZK, Ye BY, Wang ZH. 2021. Remote sensing monitoring and evaluation of vegetation restoration in grassland mining areas—a case study of the Shengli Mining Area in Xilinhot City, China. Land. 10(7):743. doi:10.3390/land10070743.

Kogan FN. 1995. Droughts of the late 1980s in the United States as derived from NOAA Polar-Orbiting satellite data. B Am Meteorol Soc. 76(5):655–668. doi:10.1175/1520-0477(1995)076<0655:DOTLIT>2.0.CO;2.

Li J, Liang JX, Wu Y, Yin SQ, Yang Z, Hu ZQ. 2021. Quantitative evaluation of ecological cumulative effect in mining area using a pixel-based time series model of ecosystem service value. Ecol Indic. 120:106873. doi:10.1016/j.ecolind.2020.106873.

Li J, Pei YQ, Zhao SH, Xiao RL, Sang X, Zhang CY. 2020. A review of remote sensing for environmental monitoring in China. Remote Sensing. 12(7):1130. doi:10.3390/rs12071130.

Liu H, Jiang Y, Misa R, Gao JH, Xia MY, Preusse A, Sroka A, Jiang Y. 2021. Ecological environment changes of mining areas around Nansi Lake with remote sensing monitoring. Environ Sci Pollut R. 28(32):44152–44164. doi:10.1007/s11356-021-13849-y.

Li J, Xu YL, Zhang CY, Guo JT, Wang XJ, Zhang YC. 2023. Unmixing the coupling influence from driving factors on vegetation changes considering spatio-temporal heterogeneity in mining areas: a case study in Xilinhot, Inner Mongolia, China. Environ Monit Assess. 195(1):224. doi:10.1007/s10661-022-10815-0.

Lv XJ, Xiao W, Zhao YL, Zhang WK, Li SC, Sun HX. 2019. Drivers of spatio-temporal ecological vulnerability in an arid, coal mining region in Western China. Ecol Indic. 106:105475. doi:10.1016/j.ecolind.2019.105475.

Lyu X, Li XB, Gong JR, Wang H, Dang DL, Dou HS, Li SK, Liu SY. 2020. Comprehensive grassland degradation monitoring by remote sensing in Xilinhot, Inner Mongolia, China. Sustainability. 12(9):3682. doi:10.3390/su12093682.

McKenna PB, Lechner AM, Phinn S, Erskine PD. 2020. Remote sensing of mine site rehabilitation for ecological outcomes: a global systematic review. Remote Sensing. 12 (21):3535. doi:10.3390/rs12213535.

Moomen AW, Bertolotto M, Lacroix P, Jensen D. 2019. Inadequate adaptation of geospatial information for sustainable mining towards agenda 2030 sustainable development goals. J Clean Prod. 238:117954. doi:10.1016/j.jclepro.2019.117954.

Padmanaban R, Bhowmik AK, Cabral P. 2017. A remote sensing approach to environmental monitoring in a reclaimed mine area. ISPRS Int J Geo-Inf. 6(12):401. doi:10.3390/ijgi6120401.

Qin QM, You L, Zhao Y, Zhao SH, Yao YJ. 2012. Soil line automatic identification algorithm based on two-dimensional feature space. Trans CSAE. 28 (3):167–171. doi:10.3969/j.issn.1002-6819.2012.03.029. Chinese.

Qureshi S, Alavipanah SK, Konyushkova M, Mijani N, Fathololomi S, Firozjaei MK, Homaee M, Hamzeh S, Kakroodi AA. 2020. A remotely sensed assessment of surface ecological change over the gomishan wetland, Iran. Remote Sensing. 12(18):2989. doi:10.3390/rs12182989.

Rouse JW, Haas RH, Schell JA, Deering DW. 1974. Monitoring vegetation systems in the great plains with ERTS. Washington: NASA.

Roy DP, Kovalskyy V, Zhang HK, Vermote EF, Yan L, Kumar SS, Egorov A. 2016. Characterization of Landsat-7 to Landsat-8 reflective wavelength and normalized difference vegetation index continuity. Remote Sens Environ. 185:57–70. doi:10.1016/j.rse.2015.12.024.

Song W, Song W, Gu HH, Li FP. 2020. Progress in the remote sensing monitoring of the ecological environment in mining areas. Int J Env Res Pub He. 17(6):1846. doi:10.3390/ijerph17061846.

Sorek-Hamer M, Kloog I, Koutrakis P, Strawa AW, Chatfield R, Cohen A, Ridgway WL, Broday DM. 2015. Assessment of PM2.5 concentrations over bright surfaces using MODIS satellite observations. Remote Sens Environ. 163:180–185. doi:10.1016/j.rse.2015.03.014.

Sun YH, Knyazikhin Y, She XJ, Ni XN, Chen C, Ren HZ, Myneni RB. 2022. Seasonal and long-term variations in

leaf area of Congolese rainforest. Remote Sens Environ. 268:112762. doi:10.1016/j.rse.2021.112762.

Sun CJ, Li XM, Zhang WQ, Li XG. 2020. Evolution of ecological security in the tableland region of the Chinese Loess Plateau using a Remote-Sensing-Based index. Sustainability. 12(8):3489. doi:10.3390/su12083489.

Sun YH, Qin QM, Ren HZ, Zhang TY, Chen SS. 2020. Red-Edge band vegetation indices for leaf area index estimation from sentinel-2/MSI imagery. IEEE T Geosci Remote. 58(2):826–840. doi:10.1109/TGRS.2019.2940826.

Sun YH, Ren HZ, Zhang TY, Zhang CY, Qin QM. 2018. Crop leaf area index retrieval based on inverted difference vegetation index and NDVI. IEEE Geosci Remote S. 15 (11):1662–1666. doi:10.1109/LGRS.2018.2856765.

Tote C, Delalieux S, Goossens M, Williamson BJ, Swinnen E. 2014. Monitoring environmental health using SPOT-VEGETATION-derived and field-measured spectral indices in Karabash, Russia. Int J Remote Sens. 35 (13):5291–5308. doi:10.1080/01431161.2014.883103.

Vogelmann JE, Helder D, Morfitt R, Choate MJ, Merchant JW, Bulley H. 2001. Effects of Landsat 5 thematic mapper and Landsat 7 enhanced thematic mapper plus radiometric and geometric calibrations and corrections on landscape characterization. Remote Sens Environ. 78(1–2):55–70. doi:10.1016/S0034-4257(01)00249-8.

Wan Z. 2014. New refinements and validation of the collection-6 MODIS land-surface temperature/emissivity product[J]. Remote Sens Environ. 140:36–45.

Wang W, Liu RY, Gan FP, Zhou P, Zhang XW, Ding L. 2021. Monitoring and evaluating restoration vegetation status in mine region using remote sensing data: case study in Inner Mongolia, China. Remote Sensing. 13(7):1350. doi:10.3390/rs13071350.

Wu ZH, Lei SG, Lu QQ, Bian ZF, Ge SJ. 2020. Spatial distribution of the impact of surface mining on the landscape ecological health of semi-arid grasslands. Ecol Indic. 111:105996. doi:10.1016/j.ecolind.2019.105996.

Xu HQ. 2013. A remote sensing urban ecological index and its application. Acta Ecologica Sinica. 33(24):7853–7862. doi:10.5846/stxb201208301223. Chinese.

Xu HQ, Wang YF, Guan HD, Shi TT, Hu XS. 2019. Detecting ecological changes with a remote sensing based ecological index (RSEI) produced time series and change vector analysis. Remote Sensing. 11(20):2345. doi:10.3390/rs11202345.

Yang Z, Li J, Zipper CE, Shen YY, Miao H, Donovan PF. 2018. Identification of the disturbance and trajectory types in mining areas using multitemporal remote sensing images. Sci Total Environ. 644:916–927. doi:10.1016/j.scitotenv.2018.06.341.

Yiruhan A, Ma ZG, Shiyomi M. 2011. Forty-eight-year climatology of air temperature and precipitation changes in Xilinhot, Xilingol steppe (Inner Mongolia), China. Grassl Sci. 57(3):168–172. doi:10.1111/j.1744-697X.2011.00224.x.

Yu XJ. 2017. Coal mining and environmental development in southwest China. Environ Dev. 21:77–86. doi:10.1016/j.envdev.2016.12.001.

Zhang XH, Winchester N, Zhang XL. 2017. The future of coal in China. Energy Policy. 110:644–652. doi:10.1016/j.enpol.2017.07.001.

Zhang B, Wu D, Zhang L, Jiao QJ, Li QT. 2012. Application of hyperspectral remote sensing for environment monitoring in mining areas. Environ Earth Sci. 65(3):649–658. doi:10.1007/s12665-011-1112-y.

Zhang JH, Zhou ZM, Yao FM, Yang LM, Hao C. 2015. Validating the modified perpendicular drought index in the North China region using in situ soil moisture measurement. IEEE Geosci Remote S. 12(3):542–546. doi:10.1109/LGRS.2014.2349957.

Zhu Z, Wang SX, Woodcock CE. 2015. Improvement and expansion of the Fmask algorithm: cloud, cloud shadow, and snow detection for Landsats 4–7, 8, and Sentinel 2 images. Remote Sens Environ. 159:269–277. doi:10.1016/j.rse.2014.12.014.